Multigrid and Upwind Viscous Flow Solver on Three-Dimensional Overlapped and Embedded Grids

Oktay Baysal,* Kamran Fouladi,† and Victor R. Lessard†
Old Dominion University, Norfolk, Virginia 23529

A computationally efficient method is presented for solving the three-dimensional governing equations of the viscous compressible flows about complex configurations with geometrically nonsimilar components. The physical domain is decomposed into regions for which the grid generation is relatively simple and virtually without significant restrictions. The Navier-Stokes equations are solved by an implicit, upwind, finite-volume scheme. The convergence is accelerated by a multigrid algorithm despite the holes created in the computational domain by the overlapped grids, which are completely or partially embedded within one another. The block inversions and the diagonalized scalar inversions of the coefficient matrices are modified to allow the existence of such holes. The method is tested through two demonstrative cases. The solution for a supersonic flow past a blunt-nose cylinder at a high angle of attack is obtained using a C-O grid embedded in a global Cartesian grid. This solution is successfully compared with the one obtained using a single C-O grid and the experimental data. Then, supersonic interference flows past an ogive-nose cylinder in the close proximity of a flat plate are solved using overlapped and topologically nonsimilar but simple grids.

Introduction

ONE of the limitations in computational fluid dynamics is the difficulty of discretizing the physical domain around a complex three-dimensional configuration with a single grid. This task is more formidable when a configuration has multiple, joint or disjoint, and geometrically nonsimilar components. Current research efforts aim at circumventing this problem by methods such as domain decomposition or unstructured grids. A domain decomposition technique divides the flow domain into subdomains that accept easily constructed grids. In addition, such a method allows the employment of different solution methods for different subdomains.

In addition to the multiblock method, grid patching (or zonal method) and grid overlapping are the two widely used methods of domain decomposition. The zonal method requires the domain to be divided in subdomains where the grids are patched together along common boundaries. A restriction of this approach is the requirement that the patching of two zones has to be done on a surface, not a volume, and most of the time this surface has to be planar. The grid overlapping method does not require such common boundaries but does require common regions to provide the means of matching the solutions between subdomains. One subdomain can be completely or partially embedded within another. Using this concept, Steger et al.[1] developed the Chimera grid scheme. This grid scheme is flexible in selecting the subdomains such that regions of a grid common to the others can be removed, thus creating holes inside the grid. Edges of these holes represent intergrid boundaries inside a grid, and the cells contained in these holes are excluded from the calculation.

The Navier-Stokes equations are solved by an implicit, approximately factored, finite-volume, upwind and multigrid algorithm.[2,3] Baysal et al.[4] have used this algorithm to investigate supersonic flows over a blunt-nose cylinder at high angles of attack α. The objective of this paper is the extension of this algorithm to work on overlapped grids. The numerical and computational efficiency is further enhanced by employing the approximate diagonalization[5] of the coefficient matrices on overlapped grids. Multigrid convergence acceleration[6] is also built into the algorithm to work on overlapped and embedded grids. All the data structures are written in single-dimensioned arrays with pointers for efficient vectorized computer processing.[7] Therefore, the advantages of an efficient, geometrically conservative, only minimally and automatically dissipative solution algorithm are combined with the advantages and the flexibility of overlapped and embedded grids. First the method is tested by comparing the results for a simple geometry obtained with and without utilizing overlapped grids and with the experimental data.[8] Then the interference flowfields around two geometrically nonsimilar bodies[9] are solved on simple and topologically nonsimilar embedded grids.

Baseline Solution Algorithm

The governing equations are the thin-layer approximations to the Reynolds-averaged Navier-Stokes equations written in conservative form and generalized curvilinear coordinators ξ, η and ζ:

$$\partial_t Q + \partial_\xi F + \partial_\eta G + \partial_\zeta (H - H_V) = 0 \tag{1}$$

The definitions of the Cartesian (x, y, z) and generalized coordinates are shown in Fig. 1. The conserved variables per unit volume,

$$Q = [\rho, \rho u, \rho v, \rho w, e]^T \tag{2}$$

where ρ is density, e energy, and ρu, ρv, and ρw momenta, are normalized with the cylinder diameter D, the freestream values of the density, the local speed of sound, and the molecular viscosity μ. Here F, G, and H are the inviscid fluxes in ξ, η, and ζ directions, respectively, and H_V is the flux of viscous terms in ζ direction. The Sutherland formula is used to determine the molecular viscosity. The coefficient of bulk viscosity is determined through the Stokes hypothesis. The fluid is air, and it is assumed to be a perfect gas, which allows the closure for the set of equations through the perfect gas law. Reynolds stresses are modeled with an algebraic turbulence model. Further details of this formulation are given in Refs. 4 and 7.

The solution is achieved using the implicit, finite-volume, upwind algorithm described in Refs. 2, 3, 4, and 6. Roe flux-difference splitting is used to construct the upwind differences for the convective and pressure terms. Spatial deriva-

Received Jan. 30, 1989; revision received March 27, 1990.

*Associate Professor, Mechanical Engineering and Mechanics Department. Senior Member AIAA.

†Graduate Assistant, Mechanical Engineering and Mechanics Department. Student Member AIAA.

tives are written conservatively as flux balances across the cell. The Roe-averaged $\hat{()}$ cell interface values of fluxes are evaluated after a state variable interpolation where the primitive variables, density, velocity components u, v, and w, and pressure p are used. The diffusion terms are centrally differenced.

Spatial approximate factorization and Euler backward integration after linearization in time results in the solution through 5×5 block-tridiagonal matrix inversions in three directions. The delta form of Eq. (1) obtained in this manner is given below:

$$\left[\frac{I}{J\Delta t} + \delta_\xi(\partial_Q \hat{F})\right] * \left[\frac{I}{J\Delta t} + \delta_\eta(\partial_Q \hat{G})\right] * \left[\frac{I}{J\Delta t} + \delta_\zeta(\partial_Q \hat{H}) - \delta_\zeta^2\left(\frac{M}{Re}\partial_Q \hat{H}_V\right)\right] * \Delta Q = -R(Q^n) \tag{3}$$

The residual $R(Q^n)$ is the discretized representation of the spatial derivative terms in Eq. (1) evaluated at time level n; δ and δ^2 denote upwind and central differences, respectively; Δ denotes a finite increment; I is the unit diagonal matrix; M denotes the Mach number, and Re is the Reynolds number. The accuracy of this scheme is second order spatially and first order temporally.

To accelerate the convergence to a steady state, a sequence of grids are formed for each subdomain by deleting every other grid line on the next finer grid.[6] The rationale for this technique may be explained briefly as follows. The high-frequency error component on a given grid level has to be resolved on the same level by the solution algorithm explained above, since it does not appear on the next coarser grid due to the increased spacing. However, the remaining low-frequency error component appears as a high-frequency error on a coarser level grid, which in turn can be reduced by the same solution algorithm that is capable of resolving high-frequency errors. This procedure also helps the improvement of the overall robustness. A fixed cycling strategy is used, where a predetermined number of iterations are performed at each grid level. The values of the dependent variables Q and the residual R are passed from a finer grid to a coarser grid through volume-weighted restrictions I_i^{i+1} and $\hat{I}_i^{i+1}$,

$$Q_{i+1} = (I_i^{i+1} Q_i) = [\Sigma V \cdot \Delta Q]/\Sigma V \tag{4}$$

where V denotes the volume of a cell. Since the full solution is computed and stored on each grid level as opposed to only corrections, this is referred to as the full approximation scheme (FAS). Denoting the discrete analog of the operation in Eq. (1) by L, and the relative truncation error by E, the following equation is written,

$$L_{i+1}(Q_{i+1}) = R_{i+1} + E_{i+1} \tag{5}$$

where

$$R_{i+1} = (\hat{I}_i^{i+1} R_i) \tag{6}$$

Therefore, from Eqs. (4–6)

$$E_{i+1} = L_{i+1}(I_i^{i+1} Q_i) - \hat{I}_i^{i+1}[L_i(Q_i)] \tag{7}$$

Note that the solution on the coarse grid is driven by the fine grid and the relative truncation error between the coarse and fine grids. When the coarsest level is reached, computed corrections to ΔQ values at each level are prolonged to the next fine level through trilinear interpolations.

Algorithm for Domain Decomposition

Overlapped Grids

A composite grid, which is the union of the subdomain grids, is constructed to cover the region on which Eq. (1) is to be solved. The subdomain grids overlap, and the solutions defined on them individually are matched by interpolation. An order of hierarchial form between the grids allows the interaction of appropriate grids, simplifies the development of the data structure required for this interaction, and limits the search to locate points in other grids for the purpose of interpolation. Grids that are on level ℓ of the hierarchy G_ℓ are partially or completely embedded in grids of level $\ell-1$, may overlap other grids at level ℓ, and contain grids of level $\ell+1$ that are partially or completely embedded in them.

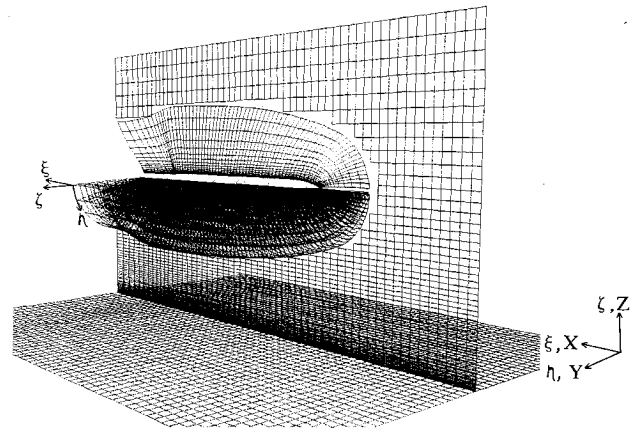

Fig. 1 Composite grid for the ogive-nose cylinder (ONC) in the proximity of a flat plate.

Following the translation and rotation of the independently generated subdomain grids to their relative positions, the cell centers are computed in the coordinate system of the composite grid. As a result of over lapping, some cells of one grid may be found to lie inside a solid boundary contained within another grid. Also, a significant number of cells must be interpolated if every cell common to more than one subdomain grid is to be updated. This is neither computationally economical nor desirable for the overall accuracy. Hence, a search method is used to create and locate the holes in each subdomain grid. This search procedure may be explained briefly here through a simple example (Fig. 2): 1) An initial hole boundary is specified as a level surface C in the embedded grid $G_{\ell+1}$. 2) Outward normals N are constructed at each hole surface cell. 3) A temporary origin P_0 of the initial hole is located by averaging the surface coordinates. 4) A maximum search radius $R_{\max}$ is defined as the maximum distance from the origin of the hole to a cell center on the hole boundary surface. 5) The initial search determines whether a cell center from grid G_ℓ lies within the search radius $R_{\max}$. If the cell center P lies within the search circle, then the next test is used. 6) Vector dot product $(N \cdot R_P)$ is computed, where R_P is the position vector to P in G_ℓ from a cell on the hole surface. If $N \cdot R_P \geq 0$, then P lies outside of the initial hole; otherwise P lies inside the initial hole and thus is defined as a hole cell in G_ℓ. A hole cell is flagged for grid G_ℓ by setting an array $IFLAG = 0$. A cell of G_ℓ that is not in the hole is flagged by setting $IFLAG = 1$.

The G_ℓ cells that are immediate neighbors of the hole cell are called the fringe cells, and the intergrid communication of the conserved variables from the $G_{\ell+1}$ grid is performed to these cells. A fringe cell is also flagged as $IFLAG = 0$. A cell in $G_{\ell+1}$ with the smallest distance to a fringe cell in G_ℓ is located and called a target cell. Then a search is conducted to find seven cells of $G_{\ell+1}$ near the target cell. The objective is to form a hexahedron that has these seven cell centers and the target point as the vertices, and this hexahedron has to include the fringe point of G_ℓ.

The information transfer from the eight cells of the $G_{\ell+1}$ grid to the fringe point of G_ℓ is done through trilinear interpolation coupled with characteristic intergrid boundary conditions. This process is called updating herein. Since trilinear interpolation can only be used on cubes, and since the hexahe-

dron formed around a target cell is generally a warped one due to the curvilinearity of a body-fitted grid, it is necessary to map a warped hexahedron to a unit cube using isoparametric mapping. The coordinates of the fringe cell that is being updated are denoted by α, b, and γ relative to its target cell. Then the interpolated values of the Q vector can be calculated as,

$$Q = a_1 + a_2\alpha + a_3\beta + a_4\gamma + a_5\alpha\beta + a_6\alpha\gamma + a_7\beta\gamma + a_8\alpha\beta\gamma \quad (8)$$

The values for the eight free variables a_i are determined from the known values of Q_i at the eight vertices of the information hexahedron. Since Eq. (8) assigns the interpolation weights without any consideration to volumes of the cells, the error is minimized by choosing the cells of the overlap regions of comparable sizes. The error is largest when interpolating from much smaller cells to a coarse cell. However, this may be corrected by incorporating the cell volumes into the weighting. This procedure is repeated in an opposite manner at the outer boundary of the overlap region, where the information is transferred from the grid G_ℓ to the grid $G_{\ell+1}$. The output of this composite grid is written in Fortran language with pointers and linked lists that appear naturally in other languages, such as Pascal or C.

An important issue in regard to the interpolation is its effect on the overall accuracy of the solution. The degree of continuity and the amount of conservation of the flow variables that can be maintained have been investigated previously (e.g., Refs. 10 and 11). An interpolation assumes the continuity of the interpolant. For the overall accuracy to be as good as the discretization formula used for Eq. (1), it is shown[10] that the width of the interpolation formula should be $0.25\ pr + 1$. In this formula, p denotes the order of the differential equation being solved, and r denotes the order of accuracy of spatial discretization. That is, two sets of fringe cells are needed for second-order accurate matching of the solutions to the second-order differential equations being solved here. The total overlap needed is given by $[d + 0.25\ pr\ (h_\ell + h_{\ell+1})]$, where h denotes a spatial step size and d denotes the distance between the innermost interpolation cell centers of grids G_ℓ and $G_{\ell+1}$. If d varies proportional to h, then the width of interpolation formula is $(0.5\ pr + 1)$. That is, third-order interpolation is needed for second-order accuracy.

The regions of high-flow gradients require approximations to the higher order derivatives of the solution, which are typically neglected. However, higher order schemes for conservative interface conditions may be unstable.[11] The remedy may be to use a conservative method of matching or simply to cluster the grid in overlap regions. A conservative method of matching is proposed in Ref. 11. A consistent approximation to the integral of conserved variables determines a matching equation being solved, if this approximation converges as the limit of h goes to zero. If this matching equation is linear, then interpolation of fluxes, as needed for conservation, is equivalent to interpolation for the solution itself. The differencing stencil required for this scheme, based upon the concept of weak solution to the differential equation, is rather irregular for three-dimensional, curvilinear grids.

Modified Solution Algorithm

Modifications are needed to use the standard block or scalar tridiagonal inversions for Eq. (3) or its approximate diagonalized counterpart, for the overlapped grids with holes. The interior computations of the subdomain grids are kept separate, and the extra work is done only at the intergrid boundaries. This allows the parallel computations of the subdomain grids in the future.[7] Therefore, the following are done to the hole or fringe cells or hole outer boundary cells: 1) set the off-diagonal 5×5 blocks in the coefficient matrix to zero, 2) set the diagonal elements of the diagonal blocks to unity, and 3) set the residuals to zero. This results in the computed

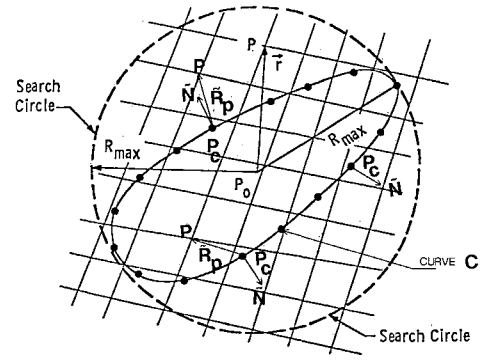

Fig. 2 Procedure for searching the hole cells created by embedded and overlapped grids.

value of ΔQ for these cells to be zero. Thus, the updated or specified boundary conditions for these cells are automatically preserved. For example, let one of the spatial factors of Eq. (3) be written as a system of algebraic equations in block tridiagonal form represented as

$$a_{ij} * \Phi_i = R_i \quad (9)$$

where a_{ij} are the 5×5 blocks of the coefficient tridigonal matrix, and Φ_i are the unknown vectors, which represents ΔQ of Eq. (3). The right-hand side residual is represented by R_i, which are the known vectors. Then,

$$R_i \leftarrow R_i * IFLAG_i \quad (10)$$

$$a_{ij} \leftarrow a_{ij} * IFLAG_i, \qquad i \neq j \quad (11)$$

$$a_{ij} \leftarrow (a_{ij} * IFLAG_i) + (1 - IFLAG_i),\ i = j \quad (12)$$

where $\leftarrow$ indicates that the left-hand side is to be replaced by the right-hand side. It should be noted that all the elements of the block a_{ij}, $i \neq j$, must become zero for the hole cells. However, only the diagonal elements must be set to unity for the diagonal blocks a_{ij}. When the approximate diagonal form is used, this process is repeated three times for each direction. The discretization for the right-hand side of Eq. (3) uses a five-point stencil for second-order spatial accuracy. To avoid the erroneous flux from a cell in a hole when computing a cell neighboring a fringe point, the Q value of the neighbor hole cell is set equal to the Q value of the fringe cell. This requires a search for such hole cells that neighbor the fringe cells in each of the three directions.

Existence of holes in the current domain decomposition method poses major problems for the implementation of a standard multigrid algorithm. The cells of the coarser level grids of each subdomain can exist everywhere, including the holes and fringe cell regions. Also, even if the cell itself is not in a hole, cells that are in a hole are conceivably used either at restrictions or prolongation stages or during the coarse-level finite-volume calculations.

First, as many coarser level grids as requested, say M, are generated from the finest level grids of each subdomain. For a grid that has a hole, say G_ℓ, the minimum IFLAG value of the eight finer level cells that make up each coarser level cell is searched. If the minimum is zero (at least one of the finer cells of this larger coarse cell is a hole cell), this coarse level cell is flagged with $IFLAGM = 0$. Otherwise, it is flagged as $IFLAGM = 1$. The M denotes the coarseness levels of the grid since this procedure is repeated for all the coarser levels. Cells as such need to be updated from the overset grid, say $G_{\ell+1}$. Therefore, a search is conducted for interpolation data [Eq. (8)] for all the points with $IFLAGM = 0$ at level M of grid G_ℓ. This search can only fail for those cells of G_ℓ at level M that lie inside, for example, the body around which the grid $G_{\ell+1}$ is

generated. Such a zone is called the illegal zone, and their cells are left with the flag $IFLAGM = 0$, so that they can be effectively excluded from this coarse-level calculation. The $IFLAGM$ values of all the other cells, which now have interpolation data, are switched from 0 to 1. The next step is locating the outer boundary connection cells of the overlap region where the interpolation is to be performed from G_ℓ to the coarser level of $G_{\ell+1}$. Such outer boundary cells of $G_{\ell+1}$, for which interpolation data are now available, are flagged as $IFLAGM = 0$. All the information obtained before for the hole cells, illegal zones, outer boundary cells, and their interpolation data is written in a data vector form for the multigrid Navier-Stokes solver. The inversions are performed at the coarser levels after the modifications are made analogous to Eqs. (10–12) with $IFLAG_i$ replaced by $IFLAGM_i$. The transfer of information between the grids, say G_ℓ and $G_{\ell+1}$, therefore, is realized through the updating performed before restrictions, and it is done over much larger physical domains than the overlap regions of the finest level meshes.

There is freedom in choosing the level grid of $G_{\ell+1}$ from which the interpolation is to be performed to the coarse level of G_ℓ. The obvious choice is searching interpolation data between the same level grids. If the cells involved in the interpolation are of comparable sizes at the finest level, as is desirable for accuracy, they are again of comparable sizes at the coarser levels. However, experience shows that the probability of success in searching for the information hexahedrons is less at a coarser level than it is with the finest level grids. Therefore, an option is built into the algorithm where the information hexahedrons are always formed from the finest level grids. This option increases the success in forming the information hexahedrons, but it decreases the accuracy. Also, this option eliminates the possibility of mesh sequencing,[4] where Eq. (1) is solved at the same coarse level of all the subdomain grids until some convergence is reached.

The prolongation stage modification may be summarized as nullifying the weight of the contributions from illegal zone cells. The prolongation is performed from the coarser cell centers, say $c1$ and $c2$, to pseudo-finer level cell centers between them, say $f1$ and $f2$ ($f1$ is closer to $c1$ than $f2$), in one direction as

$$\Delta Q_{f1} = (A1^*\Delta Q_{c1}) + (B1^*\Delta Q_{c2}) \tag{13a}$$

$$\Delta Q_{f2} = (A2^*\Delta Q_{c1}) + (B2^*\Delta Q_{c2}) \tag{13b}$$

where

$$A1 = IFLAGM_{c1}[1 - (b^*IFLAGM_{c2})] \tag{14a}$$

$$B1 = IFLAGM_{c2}[1 - (a^*IFLAGM_{c1})] \tag{14b}$$

$$A2 = IFLAGM_{c1}[1 - (a^*IFLAGM_{c2})] \tag{14c}$$

$$B2 = IFLAGM_{c2}[1 - (b^*IFLAGM_{c1})] \tag{14d}$$

and a and b are the bilinear interpolation constants (0.75 and 0.25). This process is repeated in the second direction, using the pseudo-finer level cells of the first direction. Finally, when this process is repeated in the third direction with Eq. (13) and using the pseudo-finer level cells of the second direction, the ΔQ corrections are recovered for the actual finer level cells. The resultant process is a trilinear interpolation with slight bias around an illegal zone.

Grid Construction and Boundary Conditions

The composite grid to be generated depends upon several factors among which are, the hierarchial order of the grids as demanded by the user, the width of the interpolation formula, and the stencil of the spatial differencing. The accuracy of the solution requires sufficiently smooth subdomain grids. Due to the geometric representation of the coordinate transformation, however, the finite volume method requires less smoothness of the grids than a finite difference method.

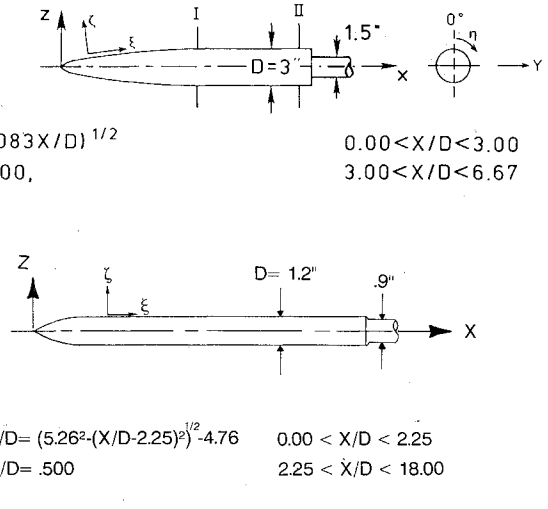

Fig. 3 Schematics of a) The blunt-nose cylinder (BNC) and b) the ogive-nose cylinder (ONC). Axial location of crossflow stations are indicated by I and II.

Two configurations are considered for the computational cases of this scheme. The first one is a blunt-nose cylinder (BNC), where the base diameter (D) is 3 in. and the length is 20 in. (Fig. 3a). A boundary-fitted C-O grid is wrapped around the BNC and this grid is embedded in a Cartesian global grid (Fig. 4). The second geometry is an ogive-nose-cylinder (ONC), in the proximity of a flat plate (Fig. 1). The base diameter and the length of the cylinder are 1.2 in. and 21.6 in., respectively (Fig. 3b). A summary of the composite grids is given in Table 1.

The Cartesian grid in Fig. 1 is drawn with the hole and the overlap region excluded. The Cartesian grid in Fig. 4 is drawn to show the hole and the overlap region. For a successful search for information hexahedrons and, hence, a connection between subdomain grids, overlaps of five to ten cells at the finest level are deemed to be necessary. A crude optimum should be found for the amount of overlap between the grids, since too much of an overlap results in unnecessary duplication of computations in these regions. The amount of skewness and warpedness may adversely affect the search and the interpolations. Various solution advancement strategies can be derived. Decisions need to be made a priori for the following: 1) the number of time steps at each coarse level grid of each subdomain grid, 2) the number of multigrid time cycles in a subdomain grid before switching to another, and 3) the number of global cycles that include all the subdomains. These numbers may be changed from one run to the other based on, for example, the reduction in L_2norm of the residuals in Eq. (3) or the time history of a flow property. Without any optimization study, the solution advancement strategy for the present results has been chosen as follows: one time step at each of the two multigrid levels of each subdomain and initially three then two multigrid V cycles in each subdomain

Table 1 Summary of the composite grids

	BNC	ONC
Cartesian grid size, ξ, η, ζ	81×73×73	97×57×73
Physical domain size in D	53×40×40	53×36×36
Number of cells with $IFLAG = 1$	426,813	401,697
Number of cells with $IFLAG = 0$	4836	1920
Number of hole boundary cells	2126	1210
C-O grid size, ξ, η, ζ	73×65×45	73×65×17
Physical domain size in D	37×4×4	37×6×6
Number of cells with $IFLAG = 1$	208,260	75,985
Number of cells with $IFLAG = 0$	5265	4680
Number of composite grid cells	645,174	484,282

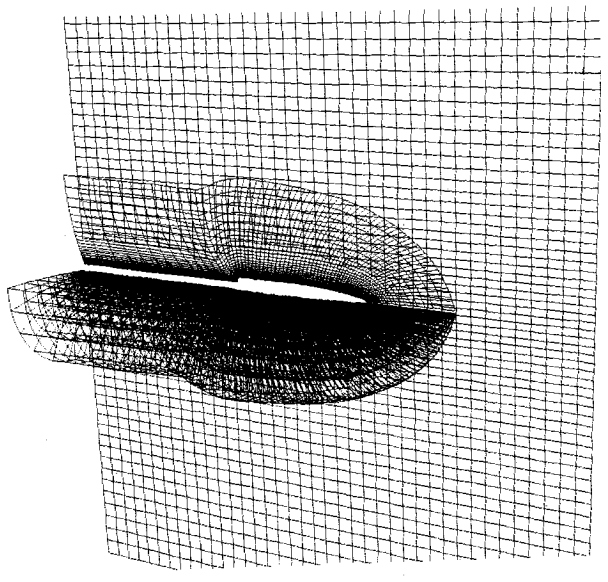

Fig. 4 Composite grid for the blunt-nose cylinder (BNC).

before switching to another. Extra computational time is expended each time the switch is made between subdomains. More multigrid cycles before the switch is computationally more efficient, but this may affect the accuracy of the results due to frozen interpolated values at the intergrid boundaries.

The boundary conditions are specified explicitly in this implicit scheme. No slip and impermeability wall boundary conditions, zero-normal gradient for wall pressure, and isothermal-wall conditions are imposed. First-order extrapolations of the conserved variables are used along the downstream boundary. The locally one-dimensional characteristic boundary conditions are specified for the top and the spanwise outboard boundaries. The upstream boundaries are all specified. A boundary-layer profile is used for the upstream of the flat plate. The cut plane of a C-mesh is treated by averaging the property values from both sides of the cut. The intergrid boundaries of a subdomain, which do not coincide with the global computational domain boundaries, are required to be updated through interpolations. This process is followed by a locally one-dimensional characteristic boundary condition check, which is performed for all the flagged intergrid boundary cells in three directions. That is, the appropriate boundary conditions are specified after the direction and the local Mach number of the flow in each cell are checked. This check is left in the code as an option, since it may be redundant for the flux-difference split solution scheme used, which is an exact solution to an approximate Riemann problem. The jump in the solution at the cell boundary is propagated in the locally correct direction and added to the existing value to get the solution at the next time step. This option, however, is necessary for a flux-vector-split[6,7] or central-differenced schemes.[1,5,7]

Results and Discussion

Two supersonic flow cases are chosen to demonstrate this computational capability. The first case is the flow past the blunt-nose cylinder with a sting at 32 deg angle of attack. The rationale for this choice is threefold: 1) a simple body-fitted grid for a body of revolution, such as a C-O grid, is topologically very different than a Cartesian grid (Fig. 4); 2) there is an available computational solution for this case that is obtained on a C-O grid only, i.e., without overlapped composite grids[4] and, 3) there are available experimental data[8] for comparisons. The flow is laminar at $M = 1.6$, $Re = 2 \times 10^6$ per foot, and the total temperature is $T_t = 585°$R. The second case is the flow past an ogive-nose cylinder with a sting in the proximity of a flat-plate wing. Since there are two components of

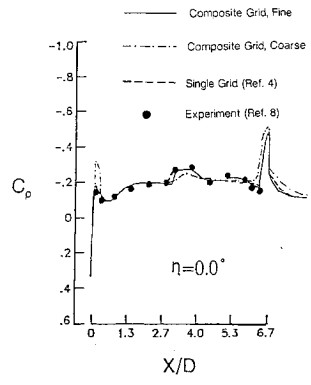

Fig. 5 Longitudinal surface pressure coefficient C_p distribution on the leeside of BNC.

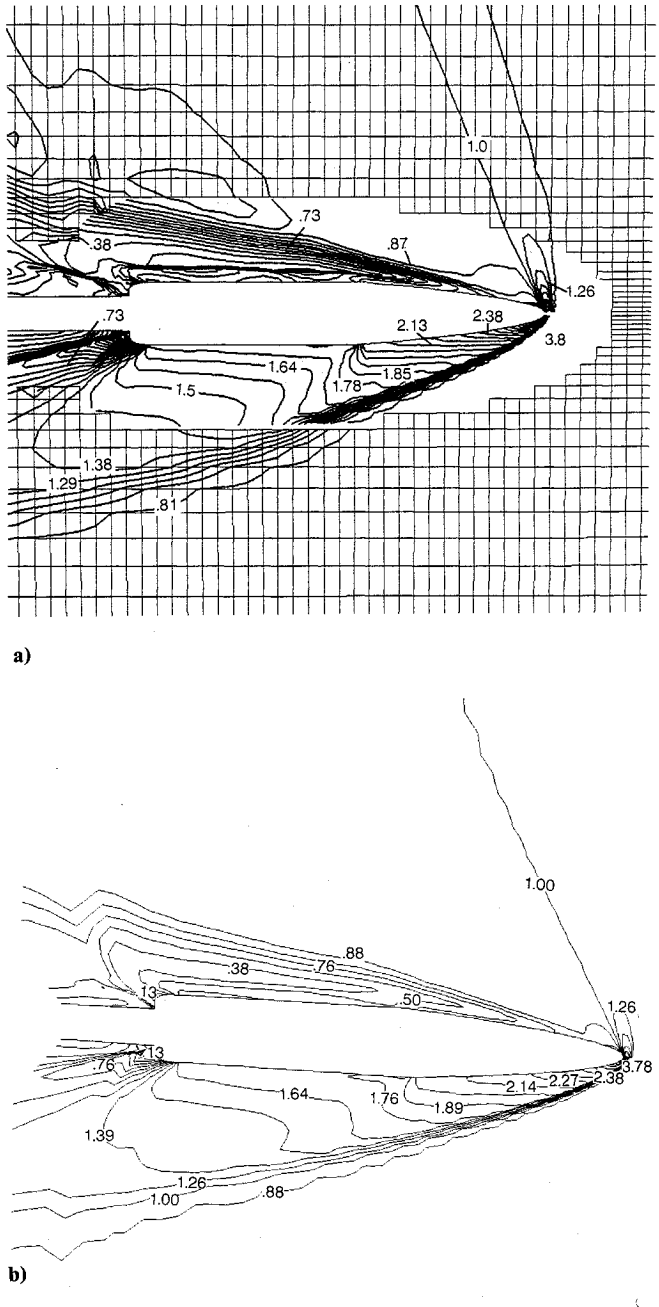

Fig. 6 Normalized pressure contours on the symmetry plane of BNC computed on a) the composite grid, and b) the single C-O grid without embedding.

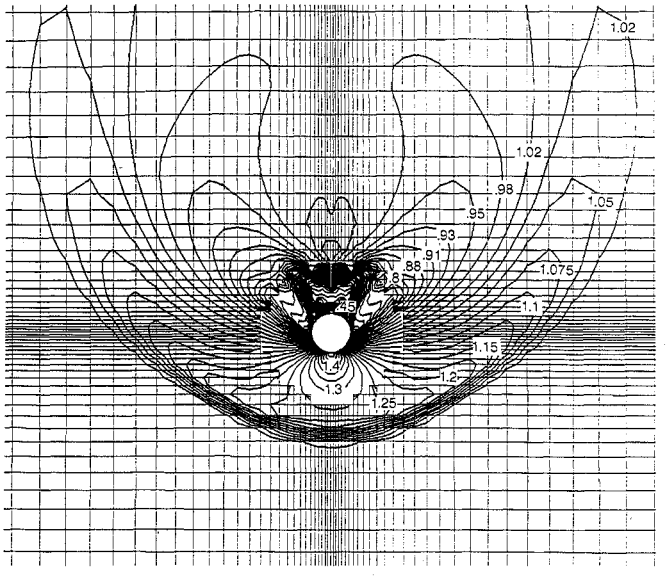

a)

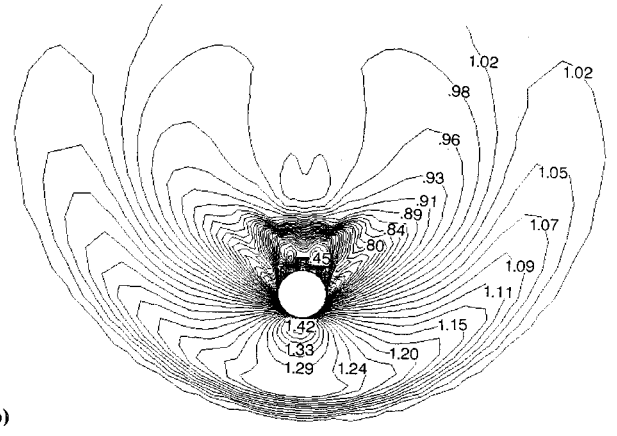

b)

Fig. 7 Normalized density contours on the crossflow Plane II of BNC computed on a) the composite grid, b) the single C-O grid without embedding.

different geometries in this configuration, employing simple grids requires the overlapped grids method. The flow is turbulent at zero angle of attack and $M = 2.86$, $Re = 2 \times 10^6$ per foot, and $T_t = 610°R$. There are alternative methods for discretizing the domain of a cylinder near a flat plate without using the present method. These methods (e.g., Refs. 12 and 13), however, cannot use simple grids such as a C-O grid and a Cartesian grid. They require three-dimensional surface grid generators. Also, either the grid interfaces have to be planar, or the grid lines going across these interfaces need to be continuous.

The longitudinal pressure coefficient C_p distribution on the leeside of BNC at $\eta = 0$ deg is shown in Fig. 5. Superimposed on the present computational results are the experimental results of Ref. 8 and the computational results of Ref. 4. The present results obtained on overlapped grids compare favorably with the experimental results. There is almost no visible difference between the present results, which are obtained on overlapped grids, and those of Ref. 4, which are obtained on a single C-O grid. In an attempt to show the effect of grid refinement on accuracy, the results obtained on overlapped coarse grids are also superimposed. As expected, the results improve with the refinement of the grid. Presented in Fig. 6 are the normalized pressure contours of the longitudinal symmetry plane. It should be noted here, when plotting in two dimensions from the three-dimensional data of different subdomains, generally one cannot find longitudinal or lateral surfaces on these subdomains that match in location or in curvature. This results in slight postprocessing discrepancies. Also, the postprocessing of the data, especially in curve fitting near intergrid boundaries, is restricted with the capabilities of the plotting programs. In any event, the contour lines cross the intergrid boundaries rather smoothly. The pressure field (Fig. 6a) compares very well with the one obtained without grid overlapping (Fig. 6b). The crossflow density contours are presented in Fig. 7. The leeside vortices are shown to pass freely through the intergrid boundary. Some minor distortions may be attributed to the fact that the Cartesian section of the crossflow surface in Fig. 7a is a planar one, as opposed to that of the single C-O grid (Fig. 7b) being a curved surface. Their trends and magnitudes, however, agree very well.

To test the effects of refinement and sequencing of overlapped grids, computations without multigrid are performed for the BNC case on the coarse grids, which are the $(41 \times 37 \times 37)$ Cartesian grid and the $(37 \times 33 \times 23)$ C-O grid (Fig. 8). Then the solution is prolonged to the fine grids, where the spatial steps are halved and the number of points are twice those of the coarse grids in each direction. The convergence history for the 900 iterations on the fine grids and without multigrid is also presented in Fig. 8. Local time stepping is used on both levels of grids with the maximum Courant number of 5. To show the effect of the multigrid computations on overlapped grids, the results of the computations on the coarse grids are restarted to use V cycles on coarse and fine grids. The solution is obtained after 900 work units. The work unit is loosely defined herein as the ratio of total CPU time used by the multigrid cycles to the CPU time needed for one iteration on the fine grids. It should be noted that the number of iterations indicated for fine grid computations is equivalent to the number of work units. The convergence rate of two-level multigrid calculations is approximately 0.98 as opposed to that of fine grid computations without multigrid, which is 0.99. If more than two levels of grids were used, the reduction of convergence rate would be more dramatic. Of course, this requires the interpolation information to be generated at more than two levels of grids. Since the number of cells in the coarse composite grid is approximately one-eighth of that of the fine composite grid, the convergence rate is better on coarse grids (approximately 0.97). This is the impetus behind performing grid sequencing before multigrid computations. However, the solution accuracy, as indicated in Fig. 5, is worse on coarse grids. The computer memory requirement increases with the number of grid levels used during multigrid cycles. The two-level multigrid computations of the BNC case require 25

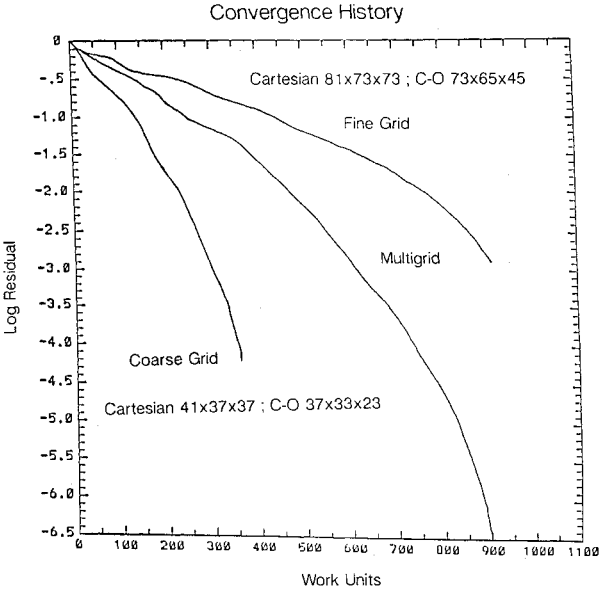

Fig. 8 Convergence histories for the computations of the BNC case.

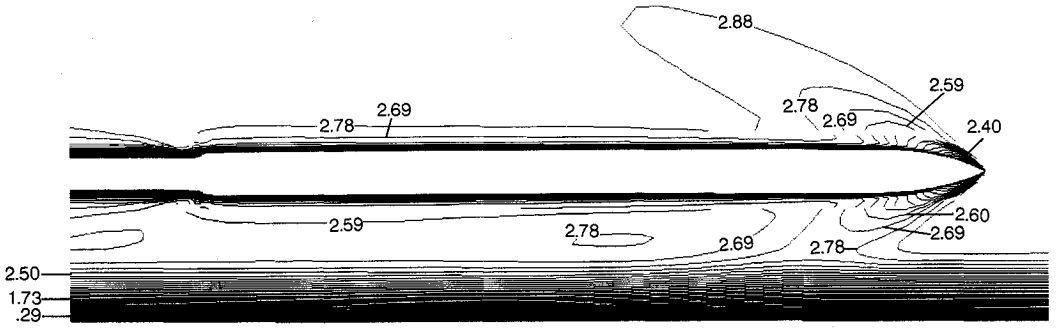

Fig. 9 Mach number contours on the symmetry plane of ONC, which is at 3.5*D* distance from the flat plate.

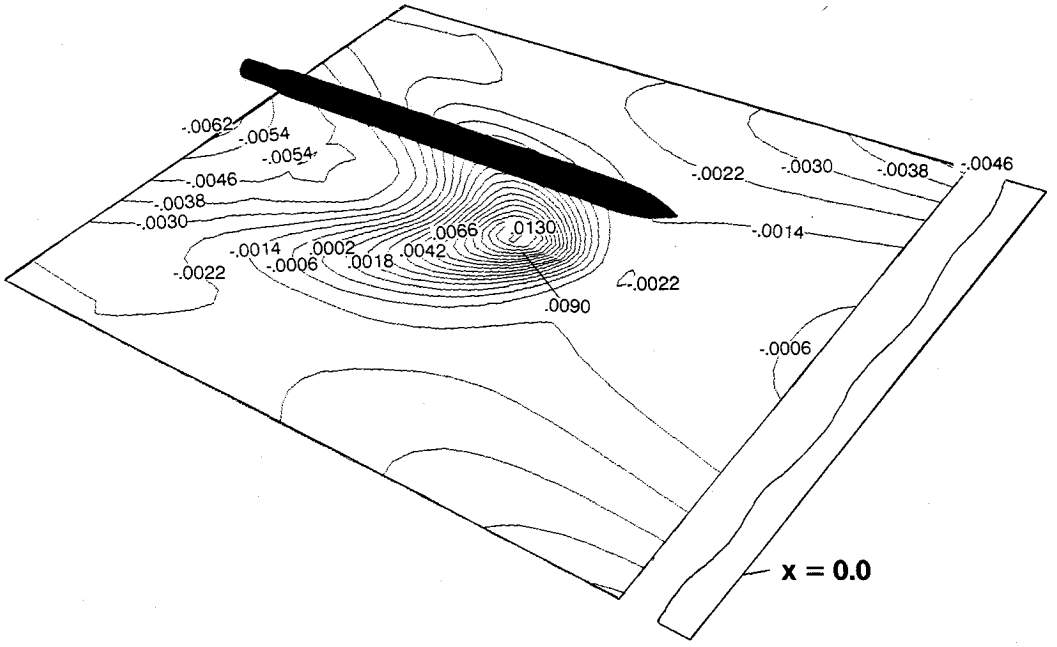

Fig. 10 Pressure coefficient contours on the surface of the flat plate with ONC at 3.5*D* distance.

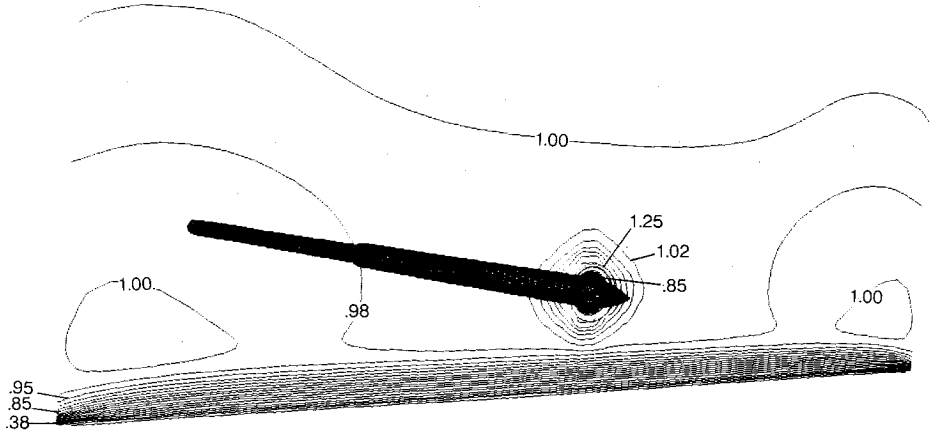

Fig. 11 Normalized density contours on the crossflow plane at forebody-cylinder junction of ONC, which is at 3.5*D* distance from the flat plate.

megawords of computer memory as opposed to 21 megawords for the fine grid computations without multigrid. All these full-precision (64-bit words) computations are performed on the CRAY-2 computer of NASA Langley Research Center.

Presented in Figs. 9–13 are the results for the flow past the ogive-nose cylinder (ONC) at 3.5*D* distance from the flat plate. The Mach number contours of the longitudinal plane of symmetry are shown in Fig. 9. The interaction of the cylinder forebody shock and the boundary layer on the flat plate is followed by the reflected recompression waves impinging on the cylinder aftbody. The influence of the reduced pressures in the region between the cylinder and the flat plate is observed as reduction of the C_p values on the flat plate (Fig. 10). They are slightly negative almost everywhere except in the region where the shock impinges. The interference of the flows is further demonstrated by the density (Fig. 11) and the Mach number (Fig. 12) contours at the cross flow plane I at forebody-cylinder junction. The shock imparts a significant mo-

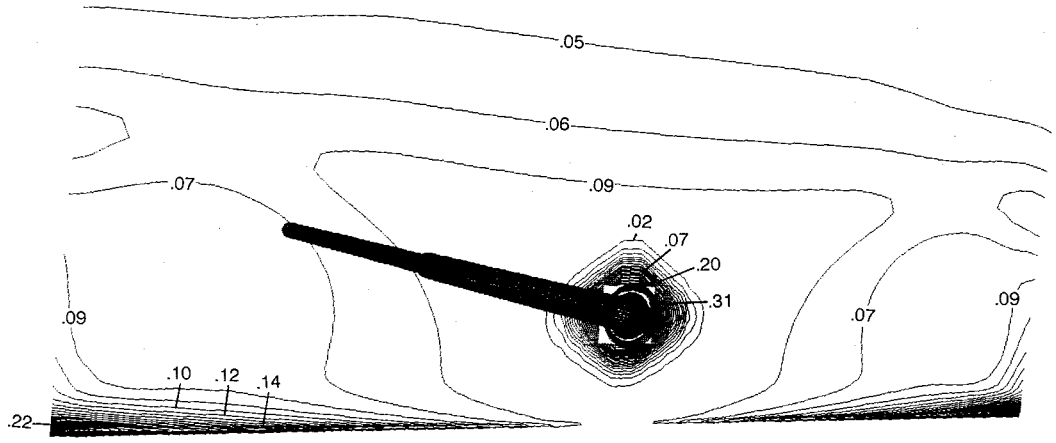

Fig. 12 Crossflow Mach number contours at forebody-cylinder junction of ONC, which is at 3.5*D* distance from the flat plate.

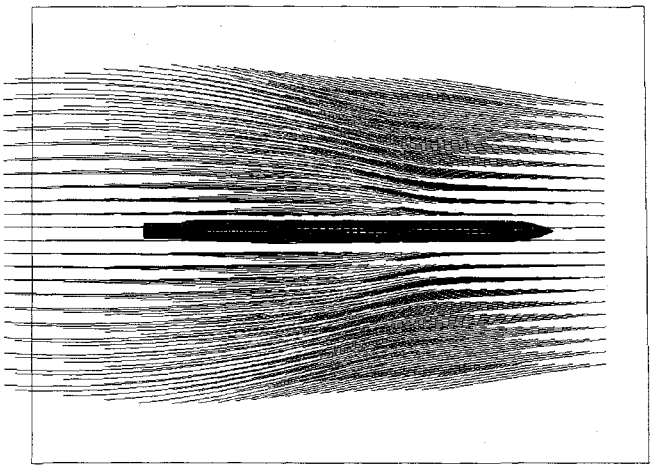

Fig. 13 Skin friction patterns on the flat plate surface with ONC at 3.5*D* distance from the flat plate.

mentum on the fluid particles in normal and spanwise directions. This can also be observed through the skin friction patterns (limiting streamlines) on the flat plate (Fig. 13). The outline of the cylinder is superimposed to indicate the relative location of the streamlines. The flow along the longitudinal centerline experiences an adverse pressure gradient (Fig. 10) until the point of shock impingement. This causes sharp spanwise turns of the streamlines with the crossflow velocities increasing, followed by inboard-direction turns to recover the freestream direction. The convergence of the limiting streamlines indicates trends of localized crossflow separations.

Conclusions

An algorithm has been developed to solve the three-dimensional, compressible, viscous flow equations for flows about complex configurations. These configurations may have multiple, joint or disjoint, and geometrically nonsimilar components. The domain decomposition method is a grid overlapping and embedding type. The solution algorithm is an implicit, upwind, finite-volume method. The multigrid convergence acceleration scheme is extended to work on overlapped and embedded grids. Therefore, the advantages of an efficient, geometrically conservative, minimally and automatically dissipative solution algorithm are combined with the advantages and flexibility of an embedded and overlapped grid scheme. The flow past an ogive-nose cylinder in the close proximity of a flat plate is solved with this method to analyze the aerodynamic interference between these bodies.

Acknowledgments

This work is supported under NASA Grant NAG-1-664. The technical monitor is D. S. Miller. The authors wish to acknowledge the helpful conservations with J. L. Thomas, J. L. Steger, F. C. Dougherty, and J. A. Benek.

References

[1]Steger, J. L., Dougherty, F. C., and Benek, J. A., "A Chimera Grid Scheme," *Advances in Grid Generation,* American Society of Mechanical Engineers, New York, FED-Vol. 5, June 1983, pp. 59–69.

[2]Thomas, J. L., Taylor, S. L., and Anderson, W. K., "Navier-Stokes Computations of Vortical Flows Over Low Aspect Ratio Wings," AIAA Paper 87-0207, Jan. 1987.

[3]Van Leer, B., Thomas, J. L., Roe, P. L., and Newsome, R. W., "A Comparison of Numerical Flux Formulas for Euler and Navier-Stokes Equations," AIAA Paper 87-1104-CP, June 1987.

[4]Baysal, O., Fouladi, K., and Miller, D. S., "Computations of Supersonic Flows Over a Body at High Angles of Attack," *AIAA Journal,* Vol. 27, No. 4, 1989, pp. 427–437.

[5]Pulliam, T. H., and Chaussee, D. S., "A Diagonal Form of an Implicit Approximate Factorization Algorithm," *Journal of Computational Physics*, Vol. 39, Feb. 1981, pp. 347–363.

[6]Anderson, W. K., and Thomas, J. L., "Multigrid Acceleration of the Flux Split Euler Equations," AIAA Paper 86-0274, Jan. 1986.

[7]Baysal, O., "Supercomputing Supersonic Flows Using Upwind Relaxation and MacCormack Schemes," *ASME Journal of Fluids Engineering,* Vol. 110, No. 1, 1988, pp. 62–68.

[8]Landrum, E. J., and Babb, C. D., "Wind-Tunnel Force, Pressure and Flow Visualization Data at Mach Numbers from 1.6 to 4.63 for a Series of Bodies of Revolution at Angles of Attack from −4° to 60°,"NASA-TM-X-3558, Oct. 1977, and NASA-TM-78813, March 1979.

[9]Stallings, R. L., Jr., "Aerodynamic Characteristics of a Sparrow III Missile Model in the Flow Field of a Generalized Parent Body at Mach 2.86," NASA-TM-85713, Feb. 1984.

[10]Henshaw, W. D., and Chesshire, G., "Multigrid on Composite Meshes," *SIAM Journal of Scientific and Statistical Computing*, Vol. 8, No. 6, 1987, pp. 914–923.

[11]Burger, M. J., "On Conservation at Grid Interfaces," *SIAM Journal of Numerical Analysis,* Vol. 24, No. 5, 1987, pp. 967–984.

[12]Belk, D. M., and Whitfield, D. L., "Time-Accurate Euler Equations Solution on Dynamic Blocked Grids," AIAA Paper 87-1127-CP, June 1987.

[13]Chow, R., and Marconi, F., "A Navier-Stokes Solution to Hypersonic Store Separation Flow Fields," AIAA Paper 89-0031, Jan. 1989.